

Heteroepitaxial Nucleation and Oriented Growth of Manganese Oxide Islands on Carbonate Minerals under Aqueous Conditions

YOUNG-SHIN JUN,
TREVOR A. KENDALL,
SCOT T. MARTIN,*
CYNTHIA M. FRIEND, AND
JOOST J. VLASSAK

Division of Engineering and Applied Sciences,
Harvard University, Cambridge, Massachusetts 02138

Manganese redox cycling and the accompanying dissolution and precipitation reactions are important processes in natural waters. In the present study, $\text{Mn}^{2+}(\text{aq})$ is reacted with $\text{O}_2(\text{aq})$ at circumneutral pH to form manganese oxide islands on the (10 $\bar{1}$ 4) surface of MnCO_3 . The islands grow heteroepitaxially. The effects of the substrate surface morphology, the substrate atomic structure, and the aqueous concentration of Mn^{2+} are investigated. On terraces, rhombohedral oxide islands form with 90° rotation relative to the crystallographic axis of the underlying carbonate substrate. Although the island heights self-limit between 2 and 3 nm depending on reaction conditions, the islands grow laterally to several square microns before separate islands collide and coalesce. The islands do not grow over substrate steps or down dissolution-pit edges. Comparison studies done with MgCO_3 and CaCO_3 show that the former also promotes heteroepitaxial growth whereas the latter does not. This difference is explained by the relative bond length mismatch between the structures of the carbonate substrates and the atomic structures of manganese oxides. A free energy model is also presented to explain why the heights of the manganese oxide islands self-limit. Our results provide an improved basis both for the development of predictive models of contaminant fate and transport and for the modeling of hydraulic flow through carbonate aquifers.

Introduction

Manganese oxide minerals in surface and groundwaters dissolve as $\text{Mn}^{2+}(\text{aq})$ and precipitate as manganese(III) and manganese(IV) oxides in response to natural and anthropogenic cycles of aqueous pE and pH conditions (1). Increases in P_{O_2} and pH favor precipitation. When precipitating, the manganese(III) and manganese(IV) oxides form thin coatings on mineral surfaces, including metal carbonates (2–4). This film formation significantly impacts the precipitation and dissolution rates in natural waters of both the substrate mineral and the manganese oxide coating. Furthermore, given the essential role of Mn as a redox active species and as a scavenger (by coprecipitation) of heavy metals (e.g., Cd

(5), Zn (6, 7), Co (8, 9), Cu (10), Ni (10), Pb (11), and As (12, 13)), manganese oxide precipitation and dissolution impact pE conditions, nutrient availability, and contaminant fate and transport. The manganese oxide films also affect the weathering of these substrates. For instance, films on carbonate minerals affect dissolution and thus provide an additional indirect impact on the alkalinity and the pH of aqueous systems and on the biogeochemical cycle of carbon. Moreover, other environmentally relevant carbonate mineral surface reactions, such as the sorption of phosphorus and trace metals, are affected (14, 15).

Although the impact of manganese oxide films on aqueous geochemistry is evident, the current understanding of the nucleation and growth mechanisms of these films under aqueous conditions is limited (1, 16, 15). Nucleation is the event in which atoms spontaneously assemble into a critically sized cluster of a thermodynamically (meta)stable phase. Growth is the process in which the cluster size increases by incorporating more atoms, thus generating larger structures (17–20). In contrast to cluster nucleation and growth from a homogeneous phase, heteroepitaxial nucleation and growth of a film is surface-directed by an underlying substrate (21). In our usage, a film describes any overgrowth on a substrate; the growth can range from two-dimensional islands, which we call a patchy film, to a contiguous sheet, which we call a continuous film. The interface between the film and the substrate has an excess energy (i.e., an interfacial energy) because the atomic positions in the interfacial region differ from their positions in relaxed reference states (e.g., in the bulk material composing the film and the substrate). The interfacial energy can limit and alter film growth (22–24).

Extensive insights into heteroepitaxial nucleation and growth have been obtained through the study of solid/gas systems at low pressure (25, 26). There is, however, correspondingly much less work and understanding of these processes for solid/aqueous systems. Atomic force microscopy (AFM) has been employed to study heteroepitaxial growth from supersaturated aqueous solutions. For example, $(\text{Pb}, \text{Sr}, \text{Cd})_x\text{Ca}_{1-x}\text{CO}_3$ and $(\text{Sr}, \text{Ba})\text{SO}_4$ two-dimensional islands form on CaCO_3 and BaSO_4 substrates, respectively, when exposed to supersaturated aqueous solutions (16, 27–29, 30). Synchrotron X-ray measurements have also been employed to study the atomic structure of several secondary precipitates, many of which are believed to form by heteroepitaxial growth from aqueous solutions (31, 32).

Our current report focuses on manganese oxide film growth on carbonate substrates under aqueous conditions. There are several earlier relevant accounts of manganese oxide film growth (33–37). Junta and Hochella's observations of manganese oxide hillocks (pH \approx 8) on hematite ($\alpha\text{-Fe}_2\text{O}_3$), goethite ($\alpha\text{-FeOOH}$), and albite ($\text{NaAlSi}_3\text{O}_8$) demonstrate that an underlying substrate provides reactive sites for the surface-catalyzed heterogeneous oxidation of Mn^{2+} and the subsequent growth of manganese oxide hillocks. The observations suggest that the initial nucleation of the manganese oxide hillocks occurs at steps and that the subsequent growth proceeds either as rows along steps (albite) or as complete surface coatings emanating from the steps (iron oxides) (35). Jun and Martin report that $\text{Mn}^{2+}(\text{aq})$ heterogeneously oxidizes on $\gamma\text{-MnOOH}$ to form a manganese oxide film that has no apparent preference for steps (36). To explain the differences between their observations and those of Junta and Hochella, in addition to comparing differences in substrates and solution conditions, Jun and Martin point to the saturation ratio as a key determinant of the characteristics of film growth. They suggest that a high saturation ratio leads to rapid growth

* Corresponding author phone: (617)495-7620; fax: (617)495-9837; e-mail: scot_martin@harvard.edu.

rates that do not allow sufficient time for surface reconstruction and energy minimization.

There are also several earlier relevant accounts of film growth on carbonate substrates (15, 37–39). Lea et al. report that $\text{Mn}_{0.5}\text{Ca}_{0.5}\text{CO}_3$ nucleates and grows heteroepitaxially on the (10 $\bar{1}$ 4) surface of CaCO_3 at pH = 8.9, 150 μM $[\text{CO}_3^{2-}]$, and $10^{-5.7}$ M added $\text{Mn}^{2+}(\text{aq})$ (15, 38). Specifically, rods of $\text{Mn}_{0.5}\text{Ca}_{0.5}\text{CO}_3$ grow parallel to the [221] direction, and the terminating faces run parallel to the [48 $\bar{1}$] and [441] directions of the CaCO_3 substrate. Adding Ca^{2+} , Mn^{2+} , and CO_3^{2-} at pH = 10.2, Astilleros et al. observe film growth on the (10 $\bar{1}$ 4) CaCO_3 surface (39). They show that, for low $[\text{Mn}^{2+}(\text{aq})]$, a $\text{Mn}_x\text{Ca}_{1-x}\text{CO}_3$ film initiates at steps, whereas at high $[\text{Mn}^{2+}(\text{aq})]$ two-dimensional nuclei form on terraces. Duckworth and Martin report the growth of a manganese oxide thin film on the (10 $\bar{1}$ 4) surface of MnCO_3 at circumneutral pH and in the presence of dissolved oxygen (1 atm O_2) (37).

Our current paper builds upon the observations of Duckworth and Martin (37) by investigating in detail the physical and chemical characteristics of the manganese oxide film. Also investigated is the dependence of the film's growth on the relationship between the atomic structure of the film and that of the substrate. Specifically, we report on the heteroepitaxial nucleation and oriented growth of manganese oxide islands on the carbonate substrates MnCO_3 , MgCO_3 , and CaCO_3 . Using atomic force microscopy, we investigate how surface morphology, aqueous manganese concentration, and substrate crystallography affect the orientation, the height, and the shape of the manganese oxide islands. We find that the islands grow on MnCO_3 terraces with a rhombohedral two-dimensional shape. On highly stepped surfaces, the islands lack a euhedral form. Addition of aqueous Mn^{2+} also distorts the rhombohedral shape. Finally, we find that the manganese oxide islands grow on MgCO_3 , but not on CaCO_3 , which we explain by bond length mismatch between the film and the substrate.

Experimental Section

Crystal Samples. MnCO_3 (rhodochrosite, sample 96030, Colorado), MgCO_3 (magnesite, sample 105090, Oberdorf, Austria), and CaCO_3 (calcite, Iceland Spar, Chilhuahua, Mexico) are selected as model metal carbonate substrates. The minerals are part of the isostructural calcite group. The crystal phase of each sample is verified using powder X-ray diffractometry (XRD, Phillips). Proton-induced X-ray emission spectroscopy (PIXE, Cambridge Particle Accelerator Facility, Harvard University) confirms the absence of significant metal impurities (detection limit of 2%) (40). Flat (10 $\bar{1}$ 4) surfaces are prepared by breaking a large (1 cm^3) crystal specimen with a razor blade. Optical images of the cleavage faces are collected using a CCD camera and digitized. The geometric sample surface area is calculated from the digital images using Photoshop CS (Adobe Systems, San Jose, CA). The typical sample surface area is 4 mm^2 . Without further treatment, samples are fixed on a steel disk with warm wax, as previously reported (36, 41).

Observation of Surface Morphology. Surface morphology is observed in contact mode using an atomic force microscope (AFM) equipped with a fluid cell (Nanoscope IIIa Multimode SPM, Digital Instruments). Images ranging from 6×6 to $13 \times 13 \mu\text{m}^2$ are recorded during 3.4 min using oxide-sharpened Si_3N_4 probes with a nominal force constant of 0.12 N m^{-1} and radius of curvature of 5 to 40 nm. Metal carbonate surfaces are reacted with solutions introduced into a fluid cell by a syringe drive (Orion Sage, Beverly, MA) at a flow rate of 0.1 mL min^{-1} . Effluent from the fluid cell is collected by a fraction collector (Retriever 500, Isco, Lincoln, NE) and analyzed off-line for aqueous manganese concentrations using a GF-AAS (Perkin-Elmer Analyst 300), from which

macroscopic dissolution rates are determined (36, 41). This setup allows real-time molecular scale observations of film growth under controlled conditions of ionic strength, pH, and saturation ratio.

Solutions. Reaction solutions are saturated with O_2 ($P_{\text{O}_2} = 1$ atm) at 298 K by purging with oxygen gas for at least 2 h. In-line moisture traps (Alltech, IL) remove CO_2 gas from the O_2 flow prior to introduction into the reaction solution. Ionic strength is adjusted with 10^{-2} M NaNO_3 (100%, Mallinckrodt).

The two main solution variables targeted for control are pH and aqueous Mn^{2+} concentration. The pH of all solutions is adjusted by addition of HNO_3 (70%, EM Science) or NaOH (98.6%, J. T. Baker). Aqueous Mn^{2+} serves as the source material for manganese oxide precipitation and derives in some experiments from MnCO_3 dissolution and in others from the external addition of a stock $\text{Mn}^{2+}(\text{aq})$ solution made at pH = 6 ± 0.2 from a sulfate salt ($\text{MnSO}_4 \cdot \text{H}_2\text{O}$).

Three complementary experimental protocols are employed: (i) MnCO_3 serves as the substrate and no $\text{Mn}^{2+}(\text{aq})$ is added, (ii) MnCO_3 is the substrate and additional $\text{Mn}^{2+}(\text{aq})$ is provided at concentrations ranging from 10^{-7} to 10^{-3} M, and (iii) CaCO_3 or MgCO_3 is the substrate and additional $\text{Mn}^{2+}(\text{aq})$ is provided at concentrations of 4×10^{-6} or 10^{-6} M, respectively. Mn solutions are prepared directly prior to the start of each experiment, and, given the slow kinetics of homogeneous Mn(II) oxidation compared to heterogeneous oxidation (i.e., Mn(II) oxidation on substrates) (42), we do not anticipate homogeneous Mn(II) oxidation to play a role in our model system. Combining protocols 1 and 2, we can interpret the effect of the aqueous Mn^{2+} concentration on island formation. The combination of protocols 1 and 3 allows us to investigate the effect of substrate crystallography on island formation. To perform oxygen control experiments for all three metal carbonate substrates, oxygen free solutions are prepared by purging solutions with argon gas. In protocol 1, in which the aqueous Mn^{2+} is derived from the substrate (e.g., MnCO_3), the starting pH is critical for reproducible results and must be slightly lower ($5.7 \leq \text{pH} \leq 6.4$) than the circumneutral range ($5.7 \leq \text{pH} \leq 8.4$) used later in the experiments. The initial lower pH values in protocol 1 are required so that sufficient $\text{Mn}^{2+}(\text{aq})$ is available, through the rapid dissolution of MnCO_3 , to initiate island nucleation.

Thermodynamic Calculations. Using the measured $[\text{Mn}^{2+}(\text{aq})]$ of the fluid cell effluent, we can calculate the saturation ratios for several solid manganese phases (oxides and carbonates) to determine which are thermodynamically possible under our experimental conditions. Calculations are completed with MINEQL+ software (Environmental Research Software, Hallowell, ME) (43) and consider the following aqueous species: Mn^{2+} , $\text{Mn}(\text{OH})^+$, $\text{Mn}(\text{OH})_2^0$, $\text{Mn}(\text{OH})_3^-$, $\text{Mn}(\text{OH})_4^{2-}$, H_2CO_3^* , HCO_3^- , CO_3^{2-} , MnHCO_3^+ , NaHCO_3^0 , HSO_4^- , NaCO_3^- , MnNO_3^+ , $\text{Mn}(\text{NO}_3)_2^0$, MnSO_4^0 , NaSO_4^- , OH^- , SO_4^{2-} , Na^+ , and NO_3^- . The MnO_4^- and MnO_4^{2-} species are omitted from the calculations because these species do not form rapidly in our pH range (i.e., $5.7 \leq \text{pH} \leq 8.4$). Results from the calculations help to constrain the composition and mineral phase of the islands that form during the experiments.

Results

At circumneutral pH and in the presence of $\text{O}_2(\text{aq})$, we find that $\text{Mn}^{2+}(\text{aq})$ oxidizes and grows heteroepitaxially as manganese oxide islands on the (10 $\bar{1}$ 4) surface of MnCO_3 . At the resolution of our AFM images, growth is observable 100 to 300 min after the introduction of the aqueous solution. The growth initially occurs as a patchy film of individual islands, which then enlarge and later coalesce into a semi-continuous film. With sufficiently long exposure (12 h) to circumneutral pH solution, the substrate surface becomes

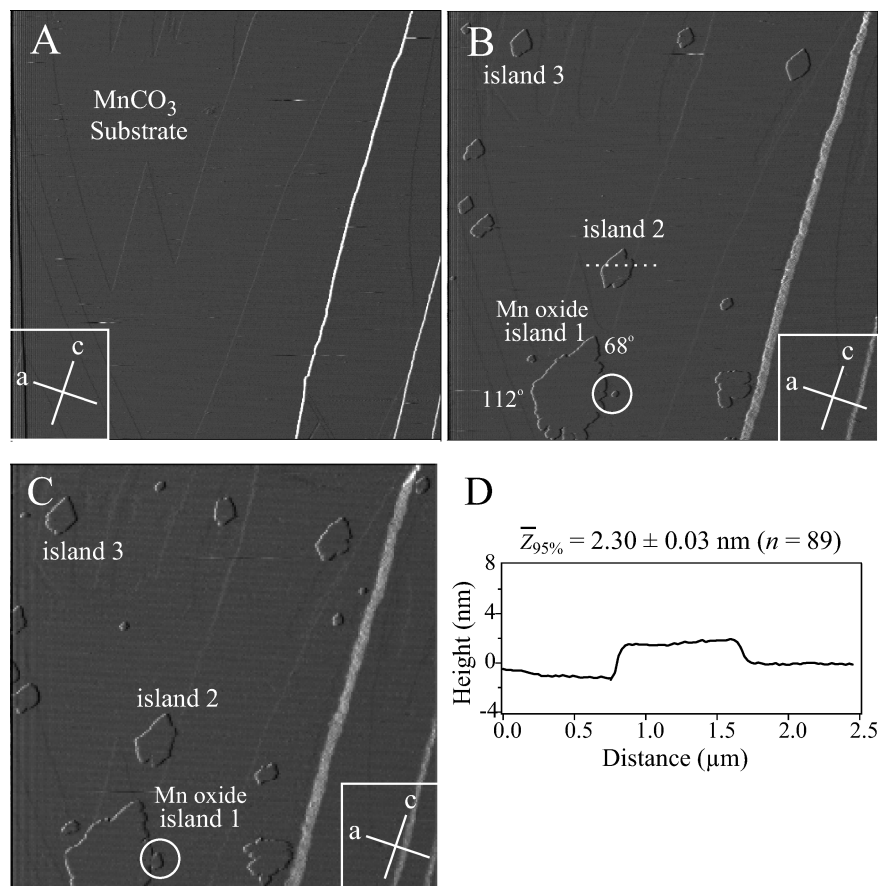


FIGURE 1. Growth of rhombohedral two-dimensional manganese oxide islands on the MnCO_3 surface. AFM micrographs are shown in deflection mode ($12 \times 12 \mu\text{m}^2$) during exposure at 298 K to a solution having $\text{pH} = 6.2$, no added aqueous Mn^{2+} , and 1 atm $\text{O}_2(\text{aq})$. The z-scale of the image is 20 nm. (A) 3 min after introduction of the aqueous solution. (B) 261 min. (C) 393 min. (D) Island height cross section, which corresponds the white dotted line in B.

fully covered with a thin manganese oxide layer. Once covered, the macroscopic dissolution rate decreases by 75% (data not shown), and no discernible microscopic surface morphology changes are observed thereafter, at least based upon 9.5 h of additional observation and so long as circumneutral pH is maintained. Film growth is, however, reversible: dissolution occurs if the pH is lowered below 5.7.

In the following sections, we report on how island growth is affected by substrate morphology, $\text{Mn}^{2+}(\text{aq})$ concentration, and substrate crystallography.

Effect of Substrate Morphology. The shape and the distribution of the islands differ when growth occurs on terraces versus on highly stepped surfaces. On terraces of MnCO_3 , rhombohedral two-dimensional manganese oxide islands nucleate and grow (Figure 1). The island heights self-limit, and the population of island heights is described by an average value of 2.3 nm and a standard deviation of 0.16 (sample size (n) of 89). The 95% confidence limit of the average of the population is 2.30 ± 0.03 nm. Given our instrument's noise floor of 0.1 nm and uncertain software corrections (e.g., to remove scanner bow), the z-directed surfaces of the islands are flat within our measurement and analysis capability (Figure 1D and cross sections shown in Figures 2, 4, 6, and 7). The statistical description of the island heights is, therefore, a convolution of the actual variability among the heights with the difficulties in measuring those heights.

In contrast to the self-limiting growth in the z-direction, the areal extent of individual islands grows with time (data not shown) and is limited on terraces only by island coalescence, which suggests that the growth is not limited in the x- and y- directions (44, 45). The lateral island dimensions begin at 60 nm when employing a 3.4 min frame

capture rate and grow steadily to several microns before islands begin to collide and coalesce (circles in Figure 1B,C). There is thus a transition from an initial patchy film of islands to a semicontinuous layer film at longer times.

The material for the growth of the manganese oxide islands is provided by the dissolution of the manganese carbonate substrate; this dissolution occurs by pit expansion and step retreat (Figure 2). When first detected, the pits are 0.3 nm deep and at least 60 nm across. The dissolution pits cluster together and remain separate from areas of initial film growth. For example, whereas precipitation preferentially occurs on the top and side areas of Figure 2C, dissolution pits are prevalent in the center. It is possible the center region of the image corresponds to a surface region having a high density of dislocations or defects, which facilitate pit formation (46). Conversely, heteroepitaxial film growth is disfavored in such surface regions because of additional lattice mismatch at the defect sites. A related possibility is that some variability in island height may be attributed to the extent of defects in the local underlying substrate.

The dissolution pits, which become detectable on the surface approximately 1 h after the introduction of the aqueous solution and after the appearance of initial island nucleation and growth, indicate the a- and c-orientations of the substrate's crystallographic axes (39). The substrate axes, when rotated 90° , also describe the apparent orientation of the islands (Figure 2A), thus demonstrating crystallographic registry between the substrate and the islands. The average inner angles of the manganese oxide islands (viz. 68.0 ± 0.6 and $112.0 \pm 0.7^\circ$, $n = 70$) are distorted by 9° from the inner angles of the MnCO_3 dissolution pits (viz. $77.0 \pm 0.4^\circ$ and $102.9 \pm 0.5^\circ$, $n = 20$). The shape of the manganese oxide

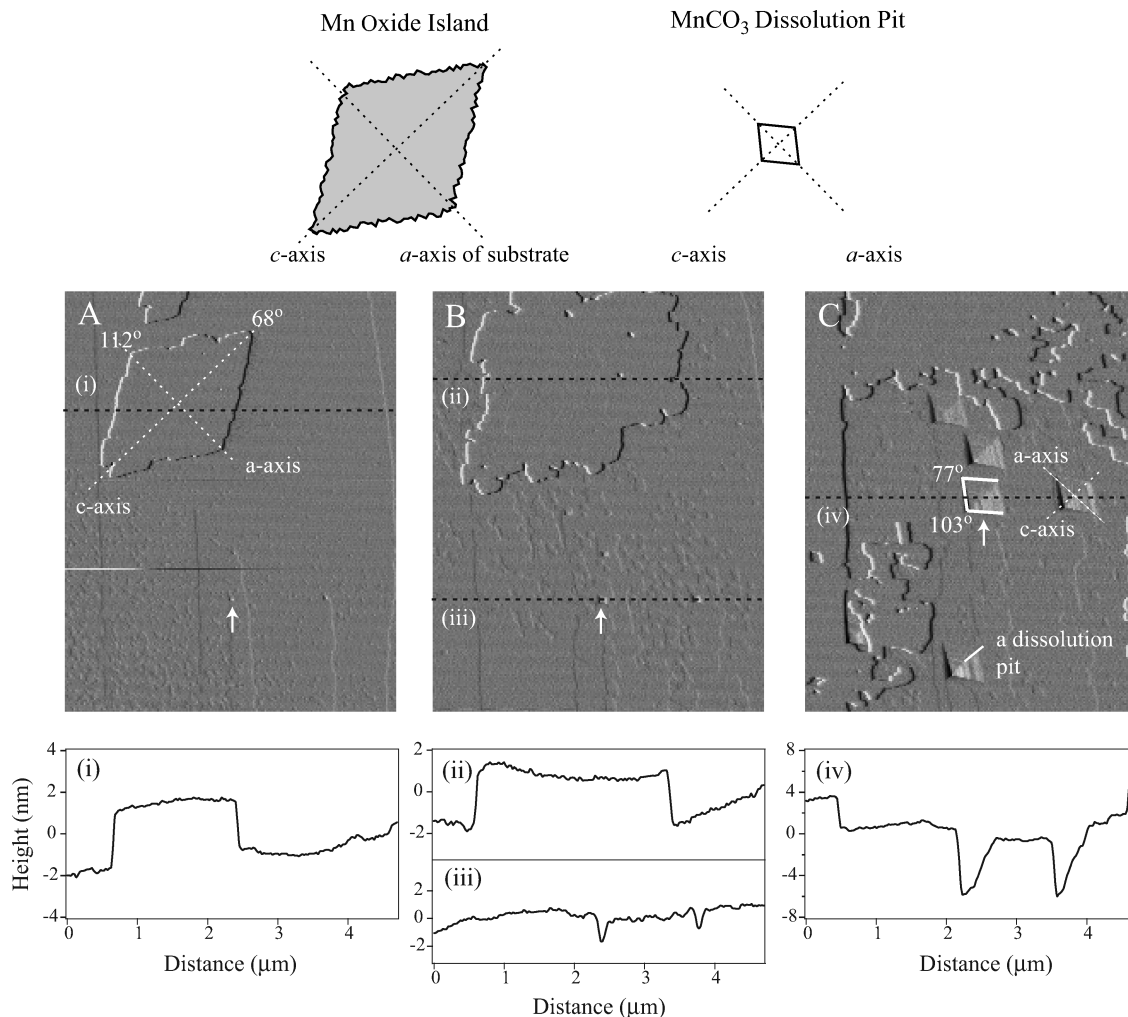


FIGURE 2. Concurrent island precipitation and substrate dissolution. **Top:** Illustration of the relative 90° rotation between the dissolution pit and the island growth. **Bottom:** (A) A rhombohedral island after 120 min exposure to solution. The island grows with 90° rotation relative to the crystallographic axis of the substrate. (B) Growth of the island after 290 min and appearance of a dissolution pit. (C) Coalescence of islands, thus forming a film, after 950 min and contemporaneous appearance of many dissolution pits. The AFM micrographs are recorded in deflection mode ($4.7 \times 6.0 \mu\text{m}^2$) at 298 K. The solution has pH = 6.1, no added aqueous Mn^{2+} , and 1 atm O_2 (aq). The z-scale of the image is 10 nm. The white arrows show a common point of reference in images A–C (image drift).

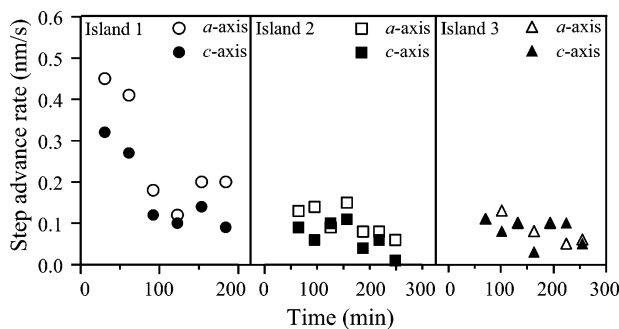


FIGURE 3. Step advance rates versus time for several islands, as labeled in Figure 1.

islands is invariant for $5.7 \leq \text{pH} \leq 6.4$, even as the macroscopic dissolution rate increases from $10^{-7.2}$ to $10^{-8.1} \text{ mol m}^{-2} \text{ s}^{-1}$. The step advance rates of three separate islands, which are labeled 1, 2, and 3 in Figure 1, are similar along the *a*- and *c*-axes ($[010]$ and $[42\bar{1}]$, respectively) (Figure 3).

As they grow, the islands do not propagate across substrate steps, an observation that is true under all explored experimental conditions. As such, steps guide and terminate island growth. The step heights on the MnCO_3 substrate range from 0.3 to 20 nm. Figure 4 provides an example in which island

growth proceeds along and toward, but not over, a 0.3 nm step. Another example is apparent in the termination of the film at the step shown in Figure 2C. In extreme cases, such as highly stepped MnCO_3 surfaces, rhombohedral islands do not form at all (Figure 5). The film growth is, instead, irregular, and a strong influence of the substrate morphology is apparent. The film thickness, however, still remains between 2 and 3 nm and does not change with time.

Effect of Mn^{2+} (aq) Concentration. The addition of aqueous Mn^{2+} , beyond the baseline concentration arising from MnCO_3 dissolution, causes an initial rounding of the rhombohedral manganese oxide islands (Figure 6A as compared to Figure 6B). Some aspects of the rhombohedral form, however, do remain, as is evident in the several straight edges still bounding some of the islands (Figure 6B). Another effect of increased Mn^{2+} (aq) concentration is an increase in the initial areal growth rate at low surface coverage from an average value of $0.5 \times 10^{-15} \text{ m}^2 \text{ s}^{-1}$ in the absence of added Mn^{2+} (aq) to one of $2.3 \times 10^{-15} \text{ m}^2 \text{ s}^{-1}$ when $10^{-5} \text{ M Mn}^{2+}$ (aq) is added. For both cases, the areal growth rate decreases with time. Notably, in the case of added Mn^{2+} (aq), when the step advance rate slows after 40 min (data not shown but similar to Figure 3), island shape reverts from rounded to rhombohedral (images not shown). A final effect of increased Mn^{2+} (aq) concentration is a slight

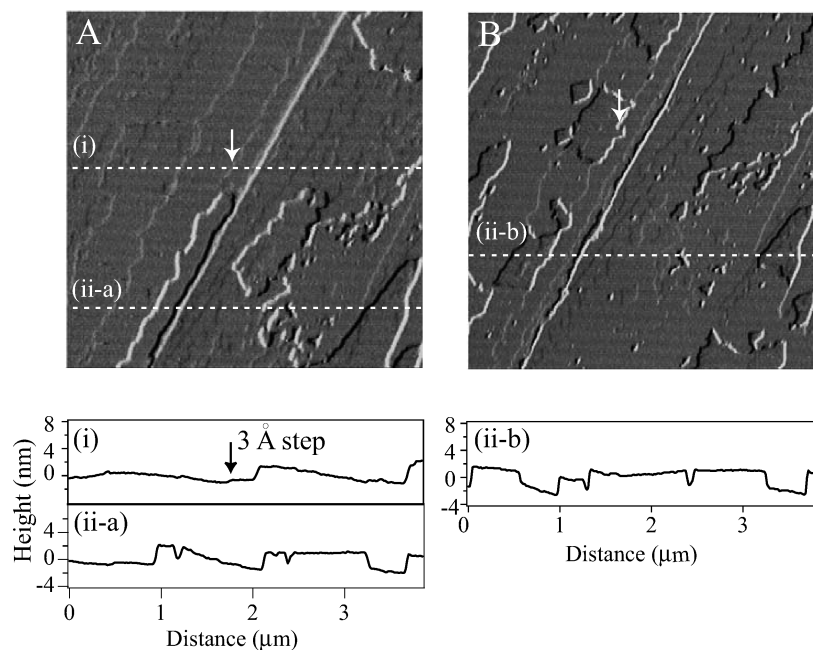


FIGURE 4. Step guides manganese oxide precipitation on a stepped MnCO_3 surface. (A) A 0.3 nm step (indicated by the white arrow) guides growth. (B) 400 min after exposure to solution. The film does not cross over a step. Micrographs A and B are recorded in deflection mode ($4 \times 4 \mu\text{m}^2$) at 298 K during exposure to a solution having pH = 6.1, no added aqueous Mn^{2+} , and 1 atm $\text{O}_2(\text{aq})$. The z-scale of each image is 10 nm. The white arrow, which appears to shift due to instrument drift, points to the same location in each image.

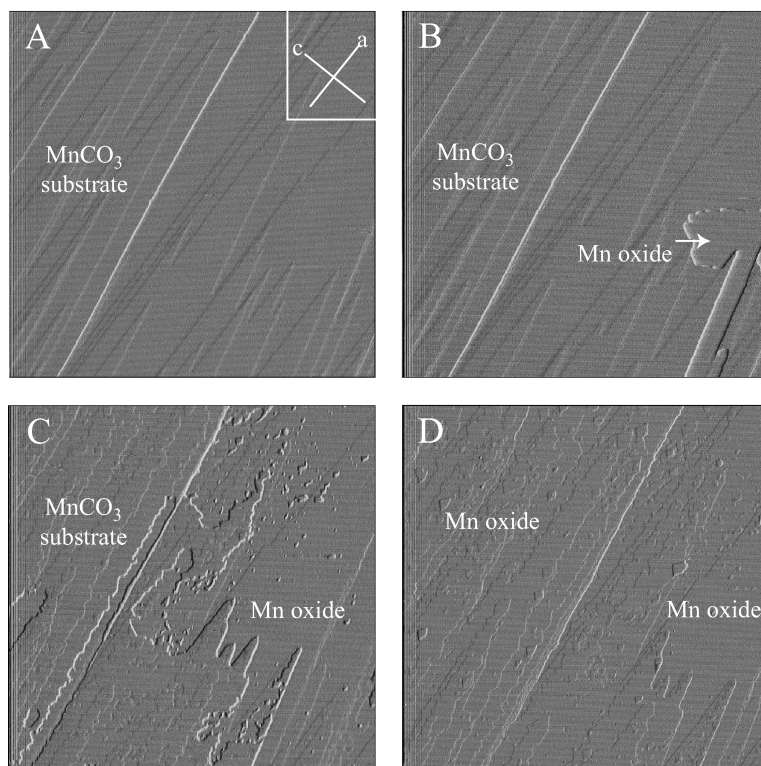


FIGURE 5. Film growth on a highly stepped surface of MnCO_3 . (A) 3 min after exposure to solution. (B) 135 min. The film growth is guided by a step. (C) 413 min. (D) 730 min. Note in the micrograph D the entire surface is covered by manganese oxide film. An image collected at 1300 min (not shown) shows no discernible changes compared to D. The micrographs A–D are shown in deflection mode ($8 \times 8 \mu\text{m}^2$). The z-scale of each image is 10 nm. See further reactor conditions in the caption of Figure 4.

thickening of island height. For example, at the highest added $\text{Mn}^{2+}(\text{aq})$ concentration of 10^{-3} M, the population of island heights is described by an average value of 2.57 nm and a standard deviation of 0.28 ($n = 20$). The 95% confidence limit of the average of the population is 2.57 ± 0.13 nm for 10^{-3} $\text{Mn}^{2+}(\text{aq})$, which compares to 2.30 ± 0.03 nm when no $\text{Mn}^{2+}(\text{aq})$ is added (next section).

Effect of Substrate Crystallography. To explore the effects of the substrate's atomic structure on the heteroepitaxial island growth, we compare our results obtained with MnCO_3 as the substrate with those obtained with MgCO_3 or CaCO_3 as the substrate. Manganese oxide islands grow on MgCO_3 in the presence of 10^{-6} M added $\text{Mn}^{2+}(\text{aq})$ and 1 atm $\text{O}_2(\text{aq})$ (Figure 7), and island heights self-limit. The 95% confidence

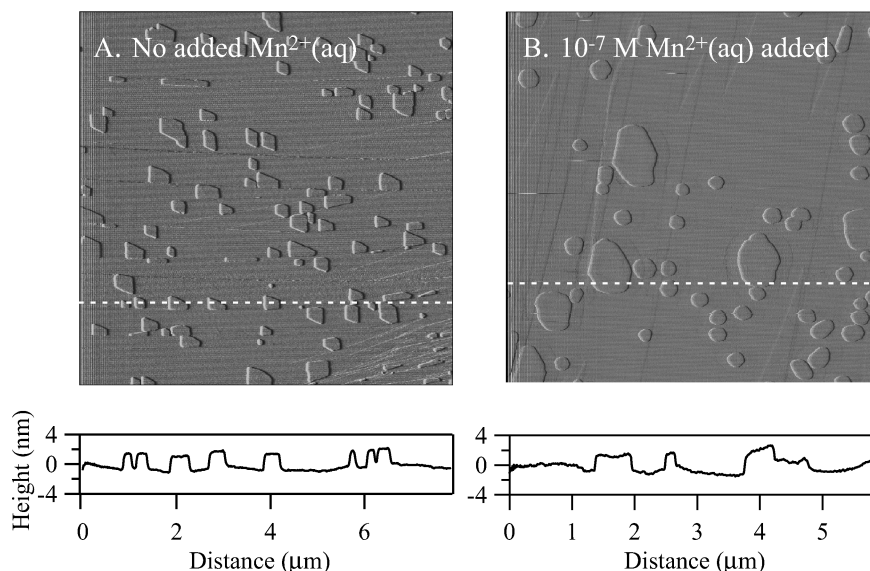


FIGURE 6. Effect of $\text{Mn}^{2+}(\text{aq})$ concentration on the shape of manganese oxide islands grown on MnCO_3 . (A) Micrograph recorded in deflection mode ($7.8 \times 7.8 \mu\text{m}^2$) and obtained 44 min after exposure to a solution having $\text{pH} = 6.4$ and no added aqueous Mn^{2+} . Rhombohedral islands are apparent. (B) Micrograph ($5.9 \times 5.9 \mu\text{m}^2$) obtained 20 min after exposure to a solution having $\text{pH} = 6.1$ and 10^{-7} M added $\text{Mn}^{2+}(\text{aq})$. The island shapes are rounded as compared to panel A. The z-scale of both images is 10 nm.

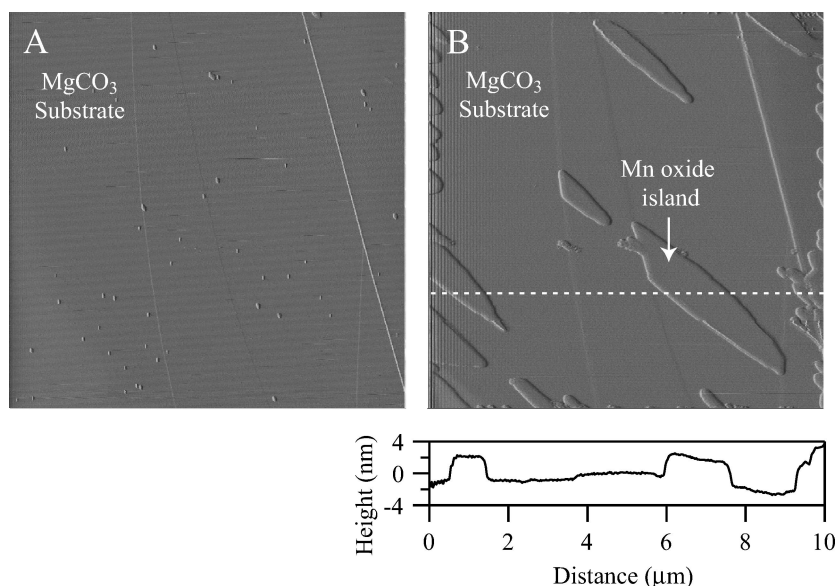


FIGURE 7. Effect of substrate chemistry on precipitation of manganese oxide islands. (A) Micrograph recorded in deflection mode ($10 \times 10 \mu\text{m}^2$) and obtained 7 min after exposure of a MgCO_3 substrate to an aqueous solution having $\text{pH} = 6.4$, 10^{-6} M $\text{Mn}^{2+}(\text{aq})$, and 1 atm $\text{O}_2(\text{aq})$. The z-scale of the image is 15 nm. Small islands are apparent. (B) 1137 min later. Manganese oxide islands grow on MgCO_3 .

limit of the average of the population of island heights is $2.46 \pm 0.05 \text{ nm}$ ($n = 60$) (standard deviation of 0.19). Unlike the rhombohedral shape observed on MnCO_3 , the island shape on the $(10\bar{1}4)$ surface of MgCO_3 is elongated (Figure 7B). The islands also appear aligned in one direction, although specific control by the underlying crystallography could not be determined because of the slow dissolution of MgCO_3 and hence the absence of dissolution pits. Although MgCO_3 steps appear to guide and terminate island growth in some cases, there are other examples in which the islands grow over large-scale morphological features at low surface coverage (Figure 7), which is in stark contrast to the regulated behavior on the MnCO_3 substrate. We also observe that, whereas some islands grow steadily, other islands shrink and eventually disappear; this ripening behavior is not observed during growth on MnCO_3 , possibly because of the infinite local supply of $\text{Mn}^{2+}(\text{aq})$ from sustained MnCO_3 dissolution. Finally, the areal growth rates of the manganese oxide islands

on MgCO_3 are six times slower than those on MnCO_3 at comparable surface coverages.

In contrast to the behavior observed with MnCO_3 and MgCO_3 , no film growth is observed when the $(10\bar{1}4)$ surface of CaCO_3 is exposed to up to $10^{-5.4} \text{ M}$ added $\text{Mn}^{2+}(\text{aq})$ and 1 atm $\text{O}_2(\text{aq})$ for $6.4 \leq \text{pH} \leq 8.4$. Changing our reaction conditions to $\text{pH} = 8.9$, $10^{-5.7} \text{ M}$ $\text{Mn}^{2+}(\text{aq})$, and $150 \mu\text{M}$ $[\text{CO}_3^{2-}]$ yields surface islands, presumably composed of $\text{Mn}^{\text{II}}_{0.5}\text{Ca}_{0.5}\text{CO}_3$ based upon the report of Lea et al. (15). In contrast to manganese oxide island growth on MnCO_3 and MgCO_3 , we find that the presence or absence of $\text{O}_2(\text{aq})$ does not affect island growth under these conditions, which supports the assignment of a Mn^{II} solid such as $\text{Mn}^{\text{II}}_{0.5}\text{Ca}_{0.5}\text{CO}_3$.

Discussion

The following analysis considers the possible chemical composition and atomic structure of the manganese oxide film. Evidence is analyzed to support the assertion that the

growth is heteroepitaxial. To explain the differences in the film's growth characteristics on several carbonate substrates, we use comparisons of the relative bond length mismatch between the structures of those substrates and the atomic structures of manganese oxides. A free energy model is also presented to explain why the heights of the manganese oxide islands self-limit.

Chemical Structure of the Film. There are several constraints on the chemical composition and the atomic structure of the film. Bulk manganese oxide and carbonate phases include (1) Mn^{II} as MnCO₃ and Mn(OH)₂; (2) Mn^{III} as β-MnOOH, γ-MnOOH, and Mn₂O₃; (3) mixed Mn^{II} and Mn^{III} as Mn₃O₄; and (4) Mn^{IV} as β-MnO₂, δ-MnO₂, and γ-MnO₂ (47). Saturation calculations rule out the formation of MnCO₃ under our experimental conditions, as follows. For 5.7 ≤ pH ≤ 8.4 in oxic solutions purged of CO₂, the total carbonate concentrations (C_T) derived from each substrate are 60 nM (MnCO₃), 1.25 nM (MgCO₃), and 6.24 μM (CaCO₃), as obtained by measuring [Mn²⁺], [Mg²⁺], and [Ca²⁺] in the reactor effluent and assuming C_T = [M²⁺]. Employing C_T, pH, and [Mn²⁺](aq), we find that the saturation ratio of MnCO₃ varies from 10^{-1.8} to 10^{-9.7} across the complete range of our experimental conditions. We thus conclude that the film is not composed of MnCO₃. Similarly, our systems are undersaturated with respect to Mn(OH)₂ for 3 < pH < 10. The requirement that O₂(aq) be present in the reaction solution also indicates that the film composition contains a higher oxidation state of manganese, thus providing further evidence against MnCO₃ and Mn(OH)₂. Previous measurements in our laboratory of the O1s XPS spectra also eliminate the possibility of a hydroxide phase (e.g., β-MnOOH and γ-MnOOH) (37). Although the saturation calculations indicate that the Mn^{IV} solid phases are thermodynamically stable under our conditions, their formation from aqueous Mn²⁺ is slow (48–50). We thus rule out hydroxides and manganese(II) and manganese(IV) oxides; we conclude that the film is a manganese(III) or a mixed manganese(II)/manganese(III) oxide.

Although saturation calculations suggest that Mn₂O₃ (bixbyite) and Mn₃O₄ (hausmannite) could form, we nevertheless rule them out based upon the following considerations. The saturation ratios of Mn₂O₃ and Mn₃O₄ approach 10⁷ and 10⁴, respectively, at pH = 6.4 and 10⁻⁵ M added Mn²⁺(aq). If the atomic positions of the film approached those of either unstrained Mn₂O₃ or Mn₃O₄, then the surface of the film would act as a nearly perfect homoepitaxial nucleus and no limitation in z-growth would occur, in disagreement with the observations. We thus rule out Mn₂O₃ and Mn₃O₄, although it is still possible that the film structure could have the crystallography of one of these solids but with a strained lattice parameter.

Our analysis thus concludes that no known, unstrained, bulk-phase manganese oxide is consistent with our experimental observations. We, therefore, hypothesize that film–substrate interactions provide a large interfacial energy contribution, which stabilizes the thin film. The strong film–substrate interactions, as implied by the limitation of island height to 2–3 nm, suggests that the islands have atomic positions and a free energy of formation different from those of bulk-phase manganese oxides. The free energy corresponding to the structure of this film is thus greater than that of bulk-phase manganese oxides. The formation of a metastable film is consistent with Ostwald's rule of stages (22). A more complete presentation of our free energy model is discussed further below. It is also possible that manganese oxide carbonate solid solutions such as Mn_aO_x(CO₃)_y and Mn_aMg_bO_x(CO₃)_y, which are not known as bulk materials, could be formed at the nanoscale.

Heteroepitaxial Growth. Our observations of the growth of euhedral manganese oxide islands on metal carbonates

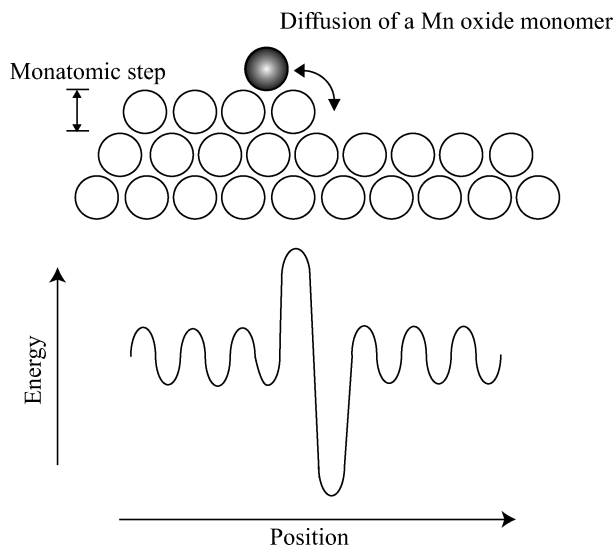


FIGURE 8. (Top) Cross-sectional depiction of a manganese oxide monomer encountering a step on a MnCO₃ surface. (Btm) Hypothesized energy profile of the diffusing monomer (Ehrlich–Schwoebel barrier) (53).

demonstrate that heteroepitaxial mechanisms are active. For instance, the influence of substrate atomic structure is shown by the rhombohedral shape of the islands (Figures 1 and 2). The rhombohedral shape is a signature mark of the atomic structure of the metal carbonate family, as revealed in the rhombohedral shape of the dissolution pits. The long axis of the manganese oxide islands is, however, rotated 90° relative to the long axis of the dissolution pits of the MnCO₃ substrate (Figure 2). The manganese oxide islands grow along the [45̄1] and [411] crystallographic directions of the MnCO₃ substrate (Figure S1). The rhombohedral form of these two directions has inner angles of 65° and 115° (51), which agree well with the inner angles observed in the AFM micrographs (viz. 68° and 112°) (Figure 2).

The addition of aqueous Mn^{II} raises the saturation ratio and, hence, increases the lateral film growth rate sufficiently that the formation of euhedral islands is hindered, as shown by the rounding in Figure 6B (19, 52). After approximately 40 min, however, as island area increases and step advance rates slow, the round shape returns to a rhombohedral form (image not shown), presumably because the surface-adsorbed monomers have sufficient time to diffuse and reorganize at the slower step advance rates. This behavior demonstrates a strong substrate effect on island growth.

Film growth is guided by steps on the substrate, and a general rule appears to hold that the film cannot cross over a step. To cross over a step, an ion pair of an advancing growth front must overcome an energy barrier caused by the undercoordination of the ion pair (Figure 8). The barrier (sometimes referred to as an Ehrlich–Schwoebel barrier) appears to be sufficiently high in the present case that thermal and diffusive variability is not large enough to overcome it with significant frequency (20, 53–55). As a result, substrate steps act as container walls to constrain and guide film growth. Hence, on a terrace, manganese oxide islands are controlled by the underlying substrate crystal structure, which results in rhombohedral structures. In comparison, at a step, heteroepitaxial growth is redirected and inhibited as islands begin to follow large-scale surface microtopography (i.e., steps), thus interrupting the potential formation of rhombohedral islands.

Role of Lattice Mismatch. Lattice mismatch, which describes the goodness-of-fit between the atomic positions of a substrate and those of a film overgrowth, plays an important role in determining whether a film grows on a

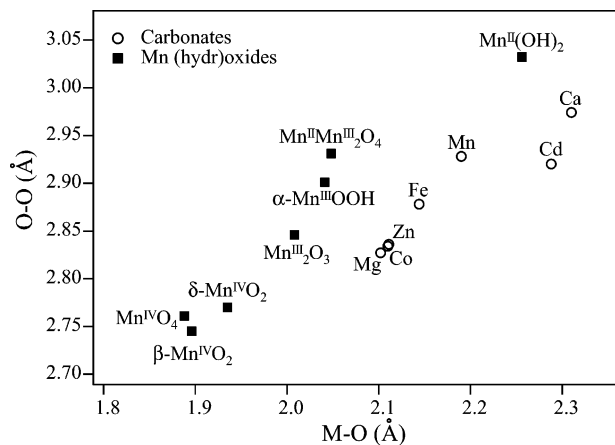


FIGURE 9. Comparison of the oxygen–oxygen and metal–oxygen bond lengths of rhombohedral carbonates to those of manganese (hydr)oxides. Oxygen–oxygen bond lengths are given as the average values. Data sources: refs 66–74.

particular substrate (20–22). Our observation of manganese oxide islands implies a small lattice mismatch between the film and the substrate. For crystals of different symmetry, a direct quantitative calculation of a lattice mismatch is difficult. As an approximation, we can calculate the percent bond length mismatch (m):

$$m = (a_A - a_B) / a_B \times 100 \quad (1)$$

where a_A and a_B are the bond lengths in the atomic structures of the island and of the substrates, respectively (Figure 9). Both the O–O and M–O bond lengths should be considered. Observations reported for alkali halides suggest that m should be less than 10–20% for efficient two-dimensional heteroepitaxial growth to occur (56).

For our system, the calculation of lattice mismatch is hindered by the absence of structural knowledge of the manganese oxide film. Our approach to this problem is to examine the clustering of the O–O and Mn–O bond lengths of the known manganese (hydr)oxide minerals (Figure 9). A reasonable assumption is that the film structure is close to that of the manganese(III) and mixed manganese(II)/manganese(III) oxides. Also shown in Figure 9 are the O–O and M–O bond lengths of the carbonate minerals. Our hypothesis is that those carbonate minerals having bond lengths similar to those of the manganese(III) oxides will be effective substrates for heteroepitaxial growth.

To test this hypothesis, we evaluate film growth on the structural endmembers (viz. CaCO_3 and MgCO_3 ; see Figure 9). Manganese oxide island growth occurs on MgCO_3 , and crystallographic control of island shape is also observed (Figure 7). In contrast, the growth of manganese oxide islands is not observed on CaCO_3 . As shown in Figure 9, the relative capabilities of the substrates to promote heteroepitaxial growth are consistent with the proximate {M–O, O–O} bond length positions of MgCO_3 and MnCO_3 versus the distant {M–O, O–O} bond length position of CaCO_3 , compared to those of the manganese(III) and mixed manganese(II)/manganese(III) oxides. Although film growth is not observed on CaCO_3 , other solids with bond lengths closer to CaCO_3 , such as $\text{Mn}_{0.5}\text{Ca}_{0.5}\text{CO}_3$, do grow heteroepitaxially (15). Even though the bond length mismatch appears to explain manganese oxide film formation on MgCO_3 and MnCO_3 and, conversely, the absence of film formation on CaCO_3 , additional factors could include differences in the adsorption isotherms of Mn^{2+} on these surfaces (57) and in the rates of heterogeneous oxidation of $>\text{Mn}^{2+}$ by O_2 at the aqueous-substrate interface (34, 42). Weak adsorption or slow heterogeneous oxidation would hinder the formation of a manganese oxide film.

Free Energy Model of Height Limitation in Island Growth. In addition to influencing whether film growth occurs, the bond length mismatch also contributes to the limitation of growth in the z -direction by affecting interfacial and strain energies. We consider three models that describe the free energy of the film as a function of thickness (L) (Figure 10). In all three models, given the planar geometry of the film, the surface-normalized volume Gibbs free energy of precipitation ($L \Delta G_V$) must decrease linearly with film thickness. In model A, the surface-normalized strain energy ($L U$) increases linearly with film thickness, which is based upon an assumption that the lattice mismatch between the film and the substrate results in a constant stress in the film. This assumption is equivalent to the statement that the atomic positions in the film structure do not vary with layer thickness. The second model (B) allows relaxation with film thickness (associated with the generation of misfit dislocations) so that the surface-normalized strain energy no longer increases beyond a critical thickness. Model B may be regarded as more realistic than model A. For both models A and B, the net change in interfacial energy ($\Delta\gamma$) due to the formation of a new surface and interface is independent of film thickness. The sum of all three energy terms ($L \Delta G_V$, $L U$, and $\Delta\gamma$) yields the total net free energy of the system (ΔG_T) with increasing layer thickness.

In model A, ΔG_T decreases linearly with film thickness, and film growth is not limited in the z -direction. In model B, an energy barrier exists in $\Delta G_T(L)$: either no film growth occurs or, if the barrier can be overcome, film growth is not limited in the z -direction. Hence, neither model A nor B can explain our observation of limited growth in the z -direction.

To explain our observations, we hypothesize that the net change in interfacial energy ($\Delta\gamma$) depends on layer thickness (model C). Experimental data for epitaxial metal films (58) and computational models for GaAs/AlAs multilayers (59) support this possibility. Physical reasoning also suggests this result: interfacial energies corresponding to a fully relaxed surface region are not possible until the material is thicker than the surface depth, which ranges from 1 to 5 nm for many bulk materials. As shown for model C in Figure 10, when $\partial(\Delta\gamma)/\partial L < -(U + \Delta G_V)$ over some finite range of layer thickness, ΔG_T goes through a minimum as the film thickness increases. Model C thus successfully rationalizes the z -limitation growth of the film. An expanded view of the energy well in model C shows that there are three regions: (i) $\partial(\Delta G_T)/\partial L < 0$ and the film grows because the driving force from more favorable interfacial energies exceeds the strain energy cost (viz. $\partial(\Delta\gamma)/\partial L < -(U + \Delta G_V)$); (ii) $\partial(\Delta G_T)/\partial L = 0$ and film growth terminates; and (iii) $\partial(\Delta G_T)/\partial L > 0$ and any putative film dissolves because the strain energy exceeds the precipitation energy $\partial(LU + L \Delta G_V)/\partial L > 0$ because $\partial(\Delta\gamma)/\partial L = 0$.

The slight thickening of the film with increasing $[\text{Mn}^{2+}](\text{aq})$ (above) can also be explained by model C. Adding Mn^{2+} decreases ΔG_V and, therefore, shifts the position of the energy well to a slightly greater thickness.

Mechanism of Heteroepitaxial Growth of a Manganese Oxide Film on Metal Carbonates. The mechanistic understanding emerging from the current work is depicted in Figure 11. Aqueous Mn^{2+} is released in the dissolution of MnCO_3 , which is accompanied on the microscale by pit expansion and step retreat. The released $\text{Mn}^{2+}(\text{aq})$ re-adsorbs to the MnCO_3 surface, which catalyzes the oxidation of $>\text{Mn}^{2+}$ by $\text{O}_2(\text{aq})$. Over the critical pH range of $5.7 \leq \text{pH} \leq 6.4$, rhombohedral manganese oxide islands nucleate and grow as a patchy film, which subsequently coalesces into a contiguous film.

The growth of the manganese oxide film is regulated by the structural controls imposed by the substrate. One

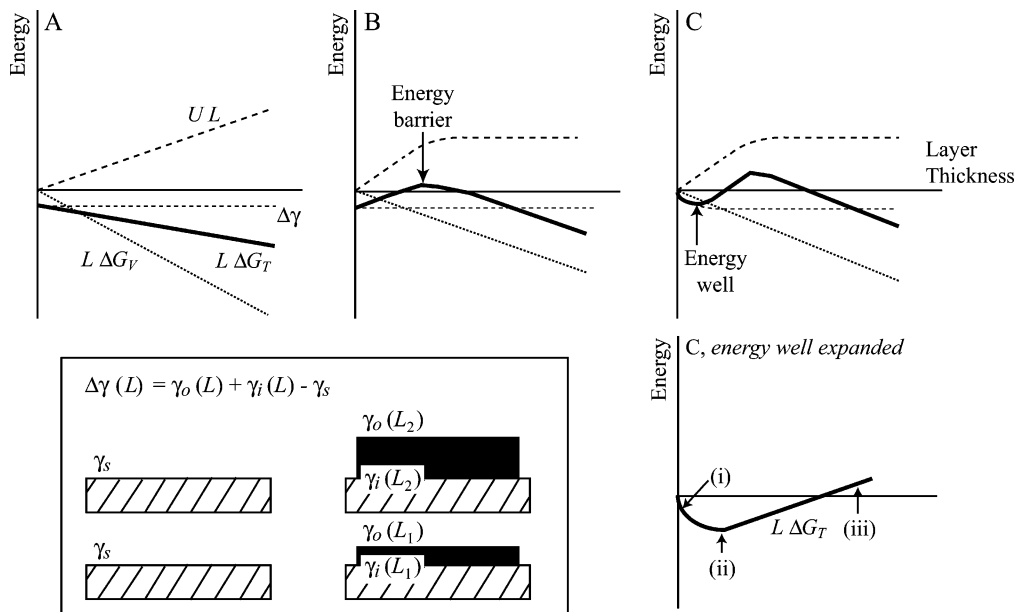
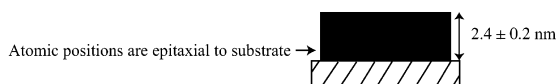
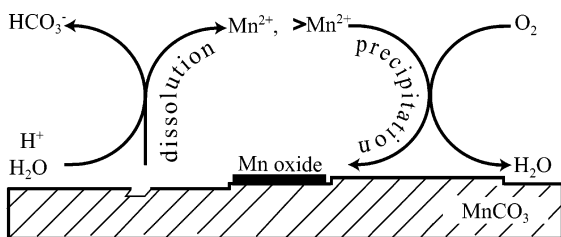
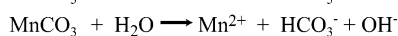


FIGURE 10. Surface-normalized energy (J m^{-2}) vs layer thickness for three model descriptions. (A) The precipitation driving force exceeds the strain energy, and the film height grows without limit. (B) The strain energy relaxes for a thicker film. After passing through an energy barrier, the film height grows without limit. (C) For a thin film, the interfacial energy can dominate. As shown in the expanded region of C, an energy well can form, and the film height can self-limit. Our observations are consistent with model C. Key: ΔG_T is the total free energy of film formation, U is the strain energy, L is the layer thickness, $\Delta\gamma$ is the net interfacial energy, and ΔG_V is the volume free energy of precipitation (i.e., $\Delta G_V = -RT \ln S$). Inset: The net interfacial energy is given by $\Delta\gamma = \gamma_o + \gamma_i - \gamma_s$ and depends on layer thickness, where γ_o is the interfacial energy of the film surface, γ_i is the interfacial energy between the film and the substrate, and γ_s is the interfacial energy of the substrate.



Step 1: Dissolution of MnCO_3



Step 2: Formation of Mn oxides



FIGURE 11. Proposed mechanism for the formation of manganese oxide islands on MnCO_3 for $5.7 < \text{pH} < 7.5$ under oxidic conditions. $>\text{Mn}^{2+}$ denotes a surface-adsorbed species.

structural control is the influence of the surface morphology. On a terrace with no steps, rhombohedral island growth occurs. In surface regions having more complex microtopography, film growth is guided and terminated by step and pit edges. A second structural control is the bond length mismatch at the substrate–film interface, which affects whether film growth occurs. For CaCO_3 , the bond length mismatch is large enough that the manganese oxide film does not form. The bond length mismatch also affects interfacial and strain energies and thus contributes to the limitation of growth in the z -direction. According to our proposed free energy model, interfacial energy, strain energy, and volume energy combine to yield an energy well, which

under our conditions corresponds to a layer thickness of 2–3 nm.

The growth of the manganese oxide film is also regulated by the chemical controls imposed by the aqueous solution. Chemical controls are observed when pH or $[\text{Mn}^{2+}(\text{aq})]$ are varied. Aqueous Mn^{2+} concentration strongly influences island shape, causing an initial rounding at high concentrations, and it weakly influences island height, causing a slight thickening with increasing concentrations.

Our observations of the heteroepitaxial growth of manganese oxide films on metal carbonate substrates provide new mechanistic insights and quantitative descriptions of the interfacial reactions between film overgrowths and substrate minerals in the environment. In particular, the atomic positions and the free energies of nanoscale films may be significantly different from bulk phase materials. These films have important consequences in system descriptions of environmental compartments: by insulating the substrate from the aqueous medium, the films impact alkalinity, the bioavailability of manganese and other divalent cations, and the phase partitioning of toxic heavy metals. Our findings provide an improved basis both for the development of predictive models of contaminant fate and transport and for the modeling of hydraulic flow through carbonate aquifers. A more detailed understanding of heteroepitaxial growth under aqueous conditions is also broadly relevant to other aspects of environmental systems, including the heterogeneously induced crystallization of ice from water in atmospheric and biological systems (60, 61) and the heterogeneously induced efflorescence of hygroscopic atmospheric particles (62–65).

Acknowledgments

We are grateful for support received from the National Science Foundation, Material Science Research Grant DMR-0213805, under the auspices of the Harvard Materials Research Science and Engineering Center; the New York Community Trust Merck Fund; the Petroleum Research Fund; the Chemical

Sciences, Geosciences, and Biosciences Division of the Office of Basic Energy Sciences in the U.S. Department of Energy; and the Harvard University Mineralogical Museum. We wish to thank Philip Gschwend, Owen Duckworth, Hui-Ming Hung, and Julie Schlenker for valuable discussion.

Supporting Information Available

Figure S1 provides a structural model of a manganese oxide island on the (10 $\bar{1}$ 4) surface of MnCO₃. This material is available free of charge via the Internet at <http://pubs.acs.org>.

Literature Cited

- (1) Villinski, J.; O'Day, P.; Corley, T.; Conklin, M. In situ spectroscopic and solution analyses of the reductive dissolution of MnO₂ by Fe(II). *Environ. Sci. Technol.* **2001**, *35*, 1157–1163.
- (2) Brown, G. E. How minerals react with water. *Science* **2001**, *294*, 67–70.
- (3) Schlegel, M. L.; Manceau, A.; Charlet, L.; Chateigner, D.; Hazemann, J. L. Sorption of metal ions on clay minerals. III. Nucleation and epitaxial growth of Zn phyllosilicate on the edges of hectorite. *Geochim. Cosmochim. Acta* **2001**, *65*, 4155–4170.
- (4) La Force, M. J.; Hansel, C. M.; Fendorf, S. Seasonal transformations of manganese in a Palustrine emergent wetland. *Soil Sci. Soc. Am. J.* **2002**, *66*, 1377–1389.
- (5) Hem, J. D.; Lind, C. J. Coprecipitation mechanisms and products in manganese oxidation in the presence of cadmium. *Geochim. Cosmochim. Acta* **1991**, *55*, 2435–2451.
- (6) Loganathan, P.; Burau, R. G. Sorption of heavy metal ions by a hydrous manganese oxide. *Geochim. Cosmochim. Acta* **1973**, *37*, 1277–1293.
- (7) Gray, M. J.; Malati, M. A. Adsorption from aqueous solution by γ -manganese dioxide. II. Adsorption of some heavy metal cations. *J. Chem. Technol. Biotechnol.* **1979**, *29*, 135–144.
- (8) Murray, J. W. The mechanism of Co(II) oxidation on synthetic birnessite. *Geochim. Cosmochim. Acta* **1983**, *47*, 1399–1403.
- (9) Hem, J. D.; Roberson, C. E.; Lind, C. J. Thermodynamic stability of CoOOH and its coprecipitation with manganese. *Geochim. Cosmochim. Acta* **1985**, *49*, 801–810.
- (10) Hem, J. D.; Lind, C. J.; Roberson, C. E. Coprecipitation and redox reactions of manganese oxides with copper and nickel. *Geochim. Cosmochim. Acta* **1989**, *53*, 2811–2822.
- (11) Hem, J. D. In *Particulates in Water*; Kavanaugh, M. C., Leckie, J. O., Eds.; American Chemical Society: Washington, DC, 1980; Vol. 189, pp 45–72.
- (12) Jenne, E. A. In *Trace Inorganics in Water*; Baker, R. A., Ed.; American Chemical Society: Washington, DC, 1968; Vol. 73, pp 337–387.
- (13) Chiu, V. Q.; Hering, J. G. Arsenic adsorption and oxidation at manganite surfaces. I. Method for simultaneous determination of adsorbed and dissolved arsenic species. *Environ. Sci. Technol.* **2000**, *34*, 2029–2034.
- (14) Nilsson, O.; Sternbeck, J. A mechanistic model for calcite crystal growth using surface speciation. *Geochim. Cosmochim. Acta* **1999**, *63*, 217–225.
- (15) Lea, A. S.; Hurt, T. T.; El-Azab, J. E.; Amonette, J. E.; Baer, D. R. Heteroepitaxial growth of a manganese carbonate secondary nano-phase on the (10 $\bar{1}$ 4) surface of calcite in solution. *Surf. Sci.* **2003**, *524*, 63–77.
- (16) Godelitsas, A.; Astilleros, J. M.; Hallam, K. R.; Harissopoulos, S.; Putnis, A. Interaction of calcium carbonates with lead in aqueous solutions. *Environ. Sci. Technol.* **2003**, *37*, 3351–3360.
- (17) Stumm, W. *Chemistry of the Solid–Water Interface: Processes at the Mineral–Water and Particle–Water Interface in Natural Systems*; Wiley: New York, 1992.
- (18) Venables, J. A. Atomic processes in crystal growth. *Surf. Sci.* **1994**, *299/300*, 798–817.
- (19) Lasaga, A. C. *Kinetic Theory in the Earth Sciences*; Princeton University Press: New Jersey, 1998.
- (20) Pimpinelli, A.; Villain, J. *Physics of Crystal Growth*; Cambridge University Press: Cambridge, 1998.
- (21) Voifltlander, B. Fundamental processes in Si/Si and Ge/Si epitaxy studied by scanning tunneling microscopy during growth. *Surf. Sci. Rep.* **2001**, *43*, 127–254.
- (22) Markov, I. V. *Crystal Growth for Beginners: Fundamentals of Nucleation, Crystal Growth and Epitaxy*; World Scientific: River Edge, NJ, 1995.
- (23) Rudin, C. D.; Spencer, B. J. Equilibrium island ridge arrays in strained solid films. *J. Appl. Phys.* **1999**, *86*, 5530–5536.
- (24) Ketteler, G.; Ranke, W. Heteroepitaxial growth and nucleation of iron oxide films on Ru(0001). *J. Phys. Chem. B* **2003**, *107*, 4320–4333.
- (25) de Miguel, J. J.; Miranda, R. Atomic aspects in the epitaxial growth of metallic superlattices and nanostructures. *J. Phys.: Condens. Matter* **2002**, *14*, R1063–R1097.
- (26) Ratsch, C.; Venables, J. A. Nucleation theory and the early stages of thin film growth. *J. Vac. Sci. Technol. A* **2003**, *21*, S96–S109.
- (27) Pina, C. M.; Enders, M.; Putnis, A. The composition of solid solutions crystallising from aqueous solutions: The influence of supersaturation and growth mechanisms. *Chem. Geol.* **2000**, *168*, 195–210.
- (28) Astilleros, J. M.; Pina, C. M.; Fernandez-Diaz, L.; Putnis, A. Metastable phenomena on calcite {10 $\bar{1}$ 4} surfaces growing from Sr²⁺-Ca²⁺-CO₃²⁻ aqueous solutions. *Chem. Geol.* **2003**, *193*, 93–107.
- (29) Astilleros, J. M.; Pina, C. M.; Fernandez-Diaz, L.; Putnis, A. Nanoscale growth of solids crystallising from multicomponent aqueous solutions. *Surf. Sci.* **2003**, *545*, L767.
- (30) Hay, M. B.; Workman, R. K.; Manne, S. Mechanisms of metal ion sorption on calcite: Composition mapping by lateral force microscopy. *Langmuir* **2003**, *19*, 3727–3740.
- (31) Chiarello, R. P.; Sturchio, N. C.; Grace, J. D.; Geissbuhler, P.; Sorensen, L. B.; Cheng, L.; Xu, S. T. Otavite-calcite solid-solution formation at the calcite-water interface studied in situ by synchrotron X-ray scattering. *Geochim. Cosmochim. Acta* **1997**, *61*, 1467–1474.
- (32) Brown, G. E.; Sturchio, N. C. An overview of synchrotron radiation applications to low-temperature geochemistry and environmental science. *Rev. Mineral. Geochem.* **2002**, *49*, 1–115.
- (33) Davies, S. H. R. In *Geochemical Processes at Mineral Surfaces*; Davies, J. A., Hayes, K. F., Eds.; American Chemical Society: Washington, DC, 1986; pp 487–502.
- (34) Davies, S. H. R.; Morgan, J. J. Manganese(II) oxidation kinetics on metal oxide surfaces. *J. Colloid Interface Sci.* **1989**, *129*, 63–77.
- (35) Junta, J. L.; Hochella Jr., M. F. Manganese(II) oxidation at mineral surfaces: A microscopic and spectroscopic study. *Geochim. Cosmochim. Acta* **1994**, *58*, 4985–4999.
- (36) Jun, Y. S.; Martin, S. T. Microscopic observations of reductive manganite dissolution under oxic conditions. *Environ. Sci. Technol.* **2003**, *37*, 2363–2370.
- (37) Duckworth, O. W.; Martin, S. T. Role of molecular oxygen in the dissolution of siderite and rhodochrosite. *Geochim. Cosmochim. Acta* **2004**, *68*, 607–621.
- (38) Lea, A. S.; Amonette, J. E.; Baer, D. R.; Liang, Y.; Colton, N. G. Microscopic effects of carbonate, manganese, and strontium ions on calcite dissolution. *Geochim. Cosmochim. Acta* **2001**, *65*, 369–379.
- (39) Astilleros, J. M.; Pina, C. M.; Fernandez-Diaz, L.; Putnis, A. Molecular-scale surface processes during the growth of calcite in the presence of manganese. *Geochim. Cosmochim. Acta* **2002**, *66*, 3177–3189.
- (40) Duckworth, O. W.; Martin, S. T. Dissolution rates and pit morphologies of rhombohedral carbonate minerals. *Am. Mineral.* **2004**, *89*, 554–563.
- (41) Duckworth, O. W.; Martin, S. T. Connections between surface complexation and geometric models of mineral dissolution investigated for rhodochrosite. *Geochim. Cosmochim. Acta* **2003**, *67*, 1787–1801.
- (42) Wehrli, B. In *Aquatic Chemical Kinetics*; Stumm, W., Ed.; Wiley: New York, 1990; pp 311–336.
- (43) Schecher, W. D.; McAvoy, D. C. *MINEQL+: A Chemical Equilibrium Modeling System*; Environmental Research Software: Lowell, 1998.
- (44) Jesson, D. E.; Chen, G.; Chen, K. M.; Pennycook, S. J. Self-limiting growth of strained faceted islands. *Phys. Rev. Lett.* **1998**, *80*, 5156–5159.
- (45) Ranke, W.; Ritter, M.; Weiss, W. Crystal structures and growth mechanism for ultrathin films of ionic compound materials: FeO(111) on Pt(111). *Phys. Rev. B* **1999**, *60*, 1527–1530.
- (46) Sangwal, K. *Etching of Crystals: Theory, Experiment, and Application*; North-Holland: New York, 1987.
- (47) Lindsay, W. L. *Chemical Equilibria in Soils*; Wiley: New York, 1979.
- (48) Hem, J. D. Rates of manganese oxidation in aqueous systems. *Geochim. Cosmochim. Acta* **1981**, *45*, 1369–1374.
- (49) Hem, J. D.; Lind, C. J. Nonequilibrium models for predicting forms of precipitated manganese oxides. *Geochim. Cosmochim. Acta* **1983**, *47*, 2037–2046.

- (50) Murray, J. W.; Dillard, J. G.; Giovanoli, R. Oxidation of Mn(II): Initial mineralogy, oxidation state and aging. *Geochim. Cosmochim. Acta* **1985**, *49*, 463–470.
- (51) Jordan, R. B.; Higgins, S. R.; Eggleston, C. M.; Knauss, K. G.; Schmahl, W. W. Dissolution kinetics of magnesite in acidic aqueous solution, a hydrothermal atomic force microscopy (HAFM) study: Step orientation and kink dynamics. *Geochim. Cosmochim. Acta* **2001**, *65*, 4257–4266.
- (52) Teng, H. H.; Dove, P. M.; De Yoreo, J. J. Kinetics of calcite growth: Surface processes and relationships to macroscopic rate laws. *Geochim. Cosmochim. Acta* **2000**, *64*, 2255–2266.
- (53) Schwoebel, R. L.; Shipsey, E. J. Step motion on crystal surfaces. *J. Appl. Phys.* **1966**, *37*, 3682–3686.
- (54) Schwoebel, R. L. Step motion on crystal surfaces. II. *J. Appl. Phys.* **1969**, *40*, 614–618.
- (55) Camarero, J.; Cros, V.; Captan, M. J.; Alvarez, J.; Ferrer, S.; Nino, M. A.; Prieto, J. E.; Gomez, L.; Ferron, J.; Vazquez de Parga, A. L.; Gallego, J. M.; Miguel, J. J.; Miranda, R. Epitaxial growth of metals with high Ehrlich-Schwobel barriers and the effect of surfactants. *Appl. Phys. A* **1999**, *69*, 553–557.
- (56) Pashley, D. W. The study of epitaxy in thin surface films. *Adv. Phys.* **1956**, *5*, 173.
- (57) McBride, M. B. Chemisorption and precipitation of Mn^{2+} at $CaCO_3$ surfaces. *Soil Sci. Soc. Am. J.* **1979**, *43*, 693–698.
- (58) Ramaswamy, V.; Nix, W. D.; Clemens, B. M. Coherency and surface stress effects in metal multilayers. *Scr. Mater.* **2004**, *50*, 711–715.
- (59) Tiller, W. A. Fundamental aspect of film nucleation and growth. *J. Vac. Sci. Technol. A* **1989**, *7*, 1353–1359.
- (60) Szyrmer, W.; Zawadzki, I. Biogenic and anthropogenic sources of ice-forming nuclei: A review. *B. Am. Meteorol. Soc.* **1997**, *78*, 209–228.
- (61) Hung, H. M.; Malinowski, A.; Martin, S. T. Kinetics of heterogeneous ice nucleation on the surfaces of mineral dust cores inserted into aqueous ammonium sulfate particles. *J. Phys. Chem. A* **2003**, *107*, 1296–1306.
- (62) Han, J. H.; Martin, S. T. Heterogeneous nucleation of the efflorescence of $(NH_4)_2SO_4$ particles internally mixed with Al_2O_3 , TiO_2 , and ZrO_2 . *J. Geophys. Res.* **1999**, *104*, 3543–3553.
- (63) Martin, S. T.; Han, J. H.; Hung, H. M. The size effect of hematite and corundum inclusions on the efflorescence relative humidities of aqueous ammonium sulfate particles. *Geophys. Res. Lett.* **2001**, *28*, 2601–2604.
- (64) Martin, S. T.; Schlenker, J.; Chelf, J. H.; Duckworth, O. W. Structure – activity relationships of mineral dusts as heterogeneous nuclei for ammonium sulfate crystallization from supersaturated aqueous solutions. *Environ. Sci. Technol.* **2001**, *35*, 1624–1629.
- (65) Han, J. H.; Hung, H. M.; Martin, S. T. The size effect of hematite and corundum inclusions on the efflorescence relative humidities of aqueous ammonium nitrate particles. *J. Geophys. Res.* **2002**, *107*, 4086.
- (66) Graf, D. L. Crystallographic tables for the rhombohedral carbonates. *Am. Mineral.* **1961**, *46*, 1283–1316.
- (67) Satomi, K. Oxygen positional parameters of tetragonal Mn_3O_4 . *J. Phys. Soc. Jpn.* **1961**, *16*, 258.
- (68) Glasser, L. S. D.; Ingram, L. Refinement of crystal structure of groutite α - $MnOOH$. *Acta Crystallogr., Sect. B* **1968**, *B24*, 1233–1236.
- (69) Geller, S. Structure of α - Mn_2O_3 ($Mn_{0.983}Fe_{0.017}O_3$) and $(Mn_{0.37}Fe_{0.63})_2O_3$ and relation to magnetic ordering. *Acta Crystallogr., Sect. B* **1971**, *B27*, 821–828.
- (70) Effenberger, H.; Mereiter, K.; Zemann, J. Crystal-structure refinements of magnesite, calcite, rhodochrosite, siderite, smithonite, and dolomite, with discussion of some aspects of the stereochemistry of calcite type carbonates. *Z. Kristallogr.* **1981**, *156*, 233–243.
- (71) Chichagov, A. V.; Belonozhko, A. B.; Lopatin, A. L.; Dokina, T. N.; Samokhvalova, O. L.; Ushakovskaya, T. V.; Shilova, Z. V. Information computing system from structural data on minerals (Mincrust). *Kristallografiya* **1990**, *35*, 610–616.
- (72) Post, J. E.; Veblen, D. R. Crystal-structure determinations of synthetic sodium, magnesium, and potassium birnessite using TEM and the rietveld method. *Am. Mineral.* **1990**, *75*, 477–489.
- (73) Reeder, R. J. Crystal chemistry of the rhombohedral carbonates. *Rev. Mineral.* **1990**, *11*, 1–47.
- (74) Waychunas, G. A. Crystal-chemistry of oxides and oxyhydroxides. *Rev. Mineral.* **1991**, *25*, 11–68.

Received for review May 29, 2004. Revised manuscript received November 24, 2004. Accepted December 8, 2004.

ES049200R